Sedimentary Geology 439 (2022) 106216

Contents lists available at ScienceDirect

Sedimentary Geology

journal homepage: www.elsevier.com/locate/sedgeo

The role of physicochemical and biochemical processes on carbonate precipitation within the Laguna Timone maar in the Pali Aike Volcanic Field, southernmost extra-Andean Patagonia

Carolina Henríquez [a,*], Mauricio Calderón [b], Leonardo Fadel Cury [a], Gustavo Athayde [c], Sergio Carvajal [d], Poldie Oyarzún [d], Anelize Bahniuk [a]

[a] LAMIR Institute, Postgraduate Program of Geology, Federal University of Paraná, Av. Cel. Francisco. H. dos Santos 100, Curitiba, Paraná, Brazil
[b] Centro de Investigación en Tecnologías para la Sociedad, Facultad de Ingeniería, Universidad del Desarrollo, Av. Plaza 680, Las Condes, Santiago, Chile
[c] Hydrogeological Research Laboratory (LPH), Postgraduate Program of Geology, Federal University of Paraná, Av. Cel. Francisco. H. dos Santos 100, Curitiba, Paraná, Brazil
[d] Laboratorio de Análisis de Sólidos, Universidad Andres Bello, Sazié 2117, Santiago, Chile

ARTICLE INFO

Article history:
Received 7 April 2022
Received in revised form 18 July 2022
Accepted 19 July 2022
Available online 26 July 2022

Editor: Dr. Brian Jones

Keywords:
Microbialites
Carbonate rocks
Clay minerals
Hydrogeology
Climate change

ABSTRACT

Carbonate deposits and sedimentary records from lakes in southern Patagonia provides an excellent contribution in the regional environmental register. The Laguna Timone is situated within a maar of the Pali Aike Volcanic Field, a Quaternary volcano-tectonic complex in southernmost South America and represents one of hundreds of "pools" of brines developed after explosive volcanic eruptions in a periglacial environment. The lake constitutes an endorheic hydrological system where processes leading to carbonate precipitation took place under extreme physicochemical conditions and biological influences that can be explored. Laguna Timone is recharged by groundwater and sporadic episodes of precipitation (ca. 200 mm/year) and high evaporation rates are controlled by regimes of strong wind (westerlies) and seasonal solar radiation. Carbonate precipitation was studied in microbialite fragments of tufa deposits and carbonate crust located in the edge of the lake, and the mineralogy of all samples is calcite. The clay fraction of the sediment underlying the carbonates was characterized and HRTEM analysis shows that authigenic smectites have influence on calcite crystal precipitation. The positive $\delta^{18}O$ values (2.28 ‰) in thin crust layers are associated with evaporation processes. In contrast, the negative $\delta^{18}O$ values (−6.52 ‰) in the microbialites show meteoric and/or groundwater influences. The $\delta^{13}C$ (−0.43 ‰ to 2.50 ‰) values indicate physico-chemical and biochemical processes controlling the precipitation. The carbonate precipitation involves the interrelations of hydrogeological properties, climate and biological influences. Laguna Timone provides a natural laboratory for understanding mineral precipitation processes that register continuous climatic and environmental archives.

1. Introduction

Sub-recent carbonate precipitates in modern lakes are formed by a combination of physical, chemical, and biological processes. Particularly the lakes in southern Patagonia represent natural laboratories that provide unique terrestrial records of (1) climate evolution, (2) hydrology, (3) interaction of ice-sheet dynamics, (4) volcano-tectonic events, (5) erosion related to strong winds and (6) microbiological processes. In this manner, most of Patagonian lakes with carbonates are ideal places to disclose the interrelation of lithospheric, biological and atmospheric processes. Nevertheless, there are few studies due to difficult access and adverse climate conditions.

A window to study these processes is provided by lakes in endorheic basins sited in semiarid regions, as in southern extra-Andean Patagonia, which generally respond effectively to environmental and climate changes (Zolitschka et al., 2006). This is the case of Laguna Timone, which corresponds to an extinct maar of the Pali Aike Volcanic Field, is one of the few permanently water-filled lake systems offering the opportunity to carry out interdisciplinary studies. The maar was formed through explosive phreatomagmatic eruptions in middle Pleistocene times once ice caps formed during the Great Patagonian Glaciation (Rabassa et al., 2005; Ton-That et al., 1999) started to retreat. Regionally, it is postulated that cold climatic conditions were influenced by a proximal periglacial environment and that explosive eruptions were related

* Corresponding author.
E-mail address: carolinahenriquez@ufpr.br (C. Henríquez).

https://doi.org/10.1016/j.sedgeo.2022.106216
0037-0738/

to the interaction of hot basaltic magmas with the permafrost (Coronato and Rabassa, 2011; Bockheim et al., 2009).

Currently, the evidence of lake-level fluctuations at Laguna Timone, recorded by several paleo-shoreline levels, and the occurrence of carbonates, clay minerals and microbial activity make this place an exceptional site to explore the record of late Quaternary environmental changes and continuous climatic archives in an unusual and still unexplored scenario. In this contribution, we combine a variety of mineralogical and geochemical analyses of sediments, carbonates and water (Henriquez, 2021) as well as field evidence obtained during systematic collection of data in two seasons. The geological and geochemical studies at Laguna Timone contribute to the knowledge of the precipitation conditions of carbonates and authigenic clay minerals, taking advantage of the favorable local conditions, considering the contribution of the volcanic source in the lake, and the identification of microbialites under cold climate in southern Patagonia.

2. Geological setting

The Cenozoic geodynamic evolution of southernmost South America is mainly due to the interaction between three tectonic plates: South American, Antarctic, and Scotia plates. It results from: (1) Subduction of the Nazca and Antarctic Plates beneath the South American Plate and (2) transcurrent movements between the Scotia and South American Plates. The occurrence of Cenozoic mafic magmatism associated with the Pali Aike Volcanic Field (PAVF) (Fig. 1) is related to the opening of an asthenospheric window under South America in response to the subduction of the Chile Ridge under the continent (D'orazio et al., 2001, 2000; Dickinson and Snyder, 1979; Skewes and Stern, 1979). The complex geotectonic configuration of plate boundaries near the PAVF at 52°S latitude resulted in distinctive tectonic provinces (Winslow, 1983). From west to east, these units correspond to: (1) a Paleozoic metamorphic basement, intruded by the Jurassic–Miocene Patagonian Batholith exposed in the Pacific Coastal Archipelago (Herve et al., 2007); (2) the Patagonian Cordillera, constituted of Upper Jurassic to Lower Cretaceous silicic volcanic rocks (Tobifera Formation) and ophiolitic complexes of the 'Rocas Verdes' back-arc basin (Calderón et al., 2007); (3) the eastern thin-skinned 'fold-and-thrust belt' developed since the Late Cretaceous to the late Miocene (Fosdick et al., 2011); and (4) finally, the Magallanes foreland basin was affected by Neogene extensional tectonics and development of graben systems (Diraison et al., 1997).

The emplacement of the Pali Aike Volcanic Field, occurred on top of the Upper Cretaceous to Cenozoic Magallanes Basin (Zolitschka et al., 2006; Mazzarini and D'Orazio, 2003; Winslow, 1983) along the southern Patagonian rift (Corbella et al., 1996). The late Miocene to Quaternary PAVF (3.8 to 0.17 Ma) extends over an area of approximately 4500 km^2 in Argentina and Chile. Three main volcanic stages have been proposed for the generation of alkaline basalts of the PAVF (Mazzarini and D'Orazio, 2003). According D'Orazio et al. (2000), the PAVF stratigraphy was can be divided into three stratigraphic units, U1, U2 and U3. U1 is the oldest and most extensive unit, covers 83 % of the total area, and consists of planar lava flows that form a plateau. Unit U2 consists of over 450 volcanic edifices which include: spatter, scoria cones, maars, and tuff ring associated with basaltic lava flows and mantelic xenoliths (Corbella, 2002; Skewes and Stern, 1979). These occupy 15 % of the total area of the PAVF. Finally, unit U3 is the youngest and consists of scoria cones and well preserved lava flows, occurs only in the SE part of the volcanic field, and occupies only 2 % of the total area.

The maar Laguna Timone discussed in this work belongs to unit U2. The preservation of these morphologies is affected due to erosion. Laguna Timone is the result of circular emission centers that reach up to 2 km in diameter and are surrounded by a tuff ring resulting from a phreatomagmatic eruption. The high diameter of the lagoon can be indicative that this is one of the oldest maars of the PAVF (Coronato and Rabassa, 2011).

The PAVF overlies late Cenozoic marine sedimentary rocks (sandstone and shale) related to a marine transgression correspond to the oldest outcropping geological strata of the study area. Miocene fine-grained molasse sediments from the Lower Miocene tectonic uplift of the Andes, and fluvioglacial deposits from the Pliocene and Pleistocene glaciations (Zolitschka et al., 2006) are present. The volcanic field

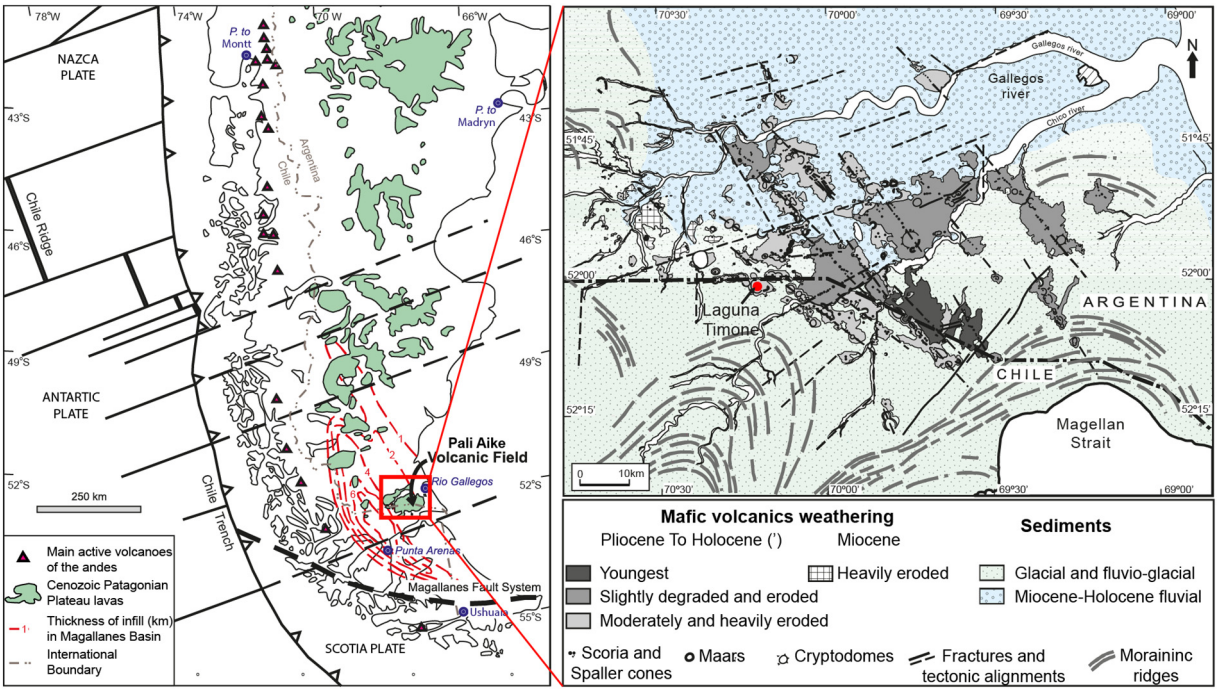

Fig. 1. Location and geologic context of the study area. The Laguna Timone maar is located near the SW border of the Pali-Aike Volcanic Field. (Source: adapted from Ross et al. (2011).)

represents the contrasting topography of a recently built eruptive area caused by glacial and periglacial phenomena, geomorphological agents of the fluvial cycle, and wind activity (Corbella and Gagliardini, 1997).

The monogenetic cones in the PAVF have a spatial distribution with a preferential alignment and elongation. The observation realized by Mazzarini and D'Orazio (2003) through the satellite image, topographic maps, field surveys, and aerial photos determines four main lineament families: N–S (azimuth range 350°–010°), NE–SW (021°–060°), E–W (080°–100°) and NW–SE (110°–150°). NW–SE and NE–SW are the most common structural orientations in the PAVF. Recent volcanism is consistent with elevated geothermal gradients (cf. Lagarrigue et al., 2019), suggesting that heat transport by advection can be related to hydrothermal fluids heated by deep and stagnant magmatic reservoirs within the continental crust.

3. Climatic conditions

Climatic conditions of southern Patagonia are controlled by Antarctic ice mass and wind circulation from the west (Weischet, 1996; Mayr et al., 2007b). High solar radiation melts extensive ice fields during the summer. Moreover, Humboldt Current (west coast) and Falkland Currents (east coast) transport cold water to the north along the Patagonian coasts, simultaneously reducing atmospheric heating. The cold-air mass advection arrives from the continent generating cold summers, and the proximity to the ocean is the cause of moderate winters (Barros et al., 1979). In general, southern Patagonia is characterized by extreme climatic conditions. Moreover, westerly winds that transport humid air from the Pacific Ocean to the Southern Andes lead to annual rainfall values between 4000 and 6000 mm on the coast and Andean territory. On the other hand, the Andean mountains behave as a topographic barrier for humid winds and generate the rain shadow on the eastern slopes of the Andes, where the PAVF is located. This fact generates an abrupt decrease in precipitation to <300 mm/year, with a regular distribution generating semi-arid and desert climates (Zolitschka et al., 2006). In addition, the decrease in relative humidity related to the increase of mean annual temperature is another factor that influences the reduction of precipitation east of the Andes (Weischet, 1996). Eastern Patagonia tends to have a continental climate dominated by the SWW, with highly evaporative conditions at the surface (Garreaud et al., 2013). In summary, the area of Laguna Timone is characterized by a semi-arid and cold climate, with temperatures close to 0 °C in winter and 15 °C in summer, characterized by regimes of strong winds and low annual precipitation rates (ca. 200 mm/year).

4. Hydrogeological description

Laguna Timone developed in the Pliocene to late Quaternary Pali Aike Volcanic Field (Zolitschka et al., 2006) and products were deposited on the volcano-sedimentary sequences of the Magallanes foreland basin (Corbella et al., 1996). Around 0.77 Ma phreatomagmatic eruptions were triggered by the interaction of mafic groundwater and/or permafrost (Zolitschka et al., 2006; Coronato and Rabassa, 2011) and formed hundreds of maars, commonly filled by a lake, creating a maar which developed into the lake of Laguna Timone. The surface of area is dominated by fluvioglacial sediments. The crater margins are formed by tuff ring forms and scoria and spatter cones. This structure contains materials generated during the eruptions such as ash, lapilli, and basalt bombs, juvenile fragments due to phreatomagmatic eruption. The crater depression of Laguna Timone, itself, is only partly occupied by the lake and has a diameter of approximately 3 km. Laguna Timone is one of the few lakes that is a permanently water-filled lacustrine system in the region. The negative topography of the maar probably allows the accumulation of water from the melting of ancient ice masses, groundwater supply and currently episodic tributaries, such as rainwater. The runoff only occurs episodically through a few arroyos after snow-melt in spring and rain episodes. The area has no permanent tributaries, no surface outflow, and semi-arid climate reflecting that the lake is fed by mainly groundwater and episodes of precipitation. Because of the pronounced exposure to the influence of westerly extremely strong winds in this area, the lake has no persistent seasonal stratification today, the winds cause frequent mixing of water levels, and therefore, the hydrological budget is extremely susceptible. Several seasonal lake-level fluctuations at Laguna Timone are evidenced by gradual withdrawal of the water in the crater, evidenced by preserved shoreline, which register a decrease in the water mass.

5. Material and methods

The applied methods focused on the materials found in shoreline. For this study, samples of carbonate rocks, sediments and water were collected during two different seasons (May and September) (Fig. 2). To have a better understanding of the lake system a schematic model was developed (Fig. 3). The lake overlaps the volcanoclastic sequence of the Magallanes basin, such as sandstones and volcanic ash associated with the Miocene Palomares Formation (Mella, 2001). The crater is filled by gravitational flow deposits associated with tuff ring erosion by winds, and carried fluvioglacial deposits. The water is dark and cloudy associated with the large number of sediment particles related to weathering of basaltic rocks, detrital material, water from the ice melting and the mixture caused by the winds. In addition to lake and carbonate-related studies, biological observations were carried out.

In the east margin of the lake, and strongly influenced by the westerlies, there is an interaction zone with waves that rework the observed microbial mats, and this material is covered and uncovered by waves. The microbial mats and biofilm are interacting with carbonate crystals. The materials are greenish to brownish, and present boomerang-shaped typical of microbial mats associated microbialites. Next, a foam is marking levels with precipitation of salts and crystals showing a strong interaction zone between the water and westerlies. A gray mud (LTS01) underlies salt crystals and carbonate crust (LT01) deposits. Then, a green sediment (LTS02) is observed inside an arroyo. This material looks like a very fine-grained mud, and it contains organic matter associated with gel-like substance characteristic of extracellular polymeric substances (EPS). In the more distal part of the lake level, deposits of tufa are found with identified microbialite fragments (LT02, LT03). The deposits have mainly botryoidal structures and in small sections aligned crystals are observed. These carbonates are not presented as tufa buildings. The deposits are highly eroded as a result of strong winds and rock falls of the volcanic deposits that surround the lake. This sector shows a notable decrease in the level of the lake. Probably, tufa deposits were larger structures covered by water.

5.1. Water physiochemistry

Water parameters such as temperature (°C), pH, electric conductivity (EC mS cm^{-1}) and total dissolved solids (TDS mg/L) through a multiparameter equipment Horiba were measured in situ during the field campaign (Table 1). The water chemistry was analyzed at *Laboratório de Pesquisas Hidrogeológicas* (LPH), housed at UFPR. The sample in the field was filtered through 0.45 μm SFCA (surfactant-free cellulose acetate) syringe filters, and the procedure was repeated due to its high content of dissolved solids. The samples were collected in the edge of the lake and superficially due to the difficulty to enter the lake. Nevertheless, the layers are constantly mixing due to strong winds (Fig. 2).

In the laboratory, the samples were filtered using a fiberglass membrane and a cellulose ester membrane. The concentrations were measured in mg/L and the abundance in milliequivalents per liter. The ion concentrations of sulfate, fluorine, phosphate, nitrites, nitrates, silica, iron and manganese using colorimetry were measured using Spectrophotometer equipment (MN® UV/Vis II). Chlorine, total alkalinity, carbonate, bicarbonate, hydroxide, calcium, and magnesium were analyzed using the analytical method Titulometry through the

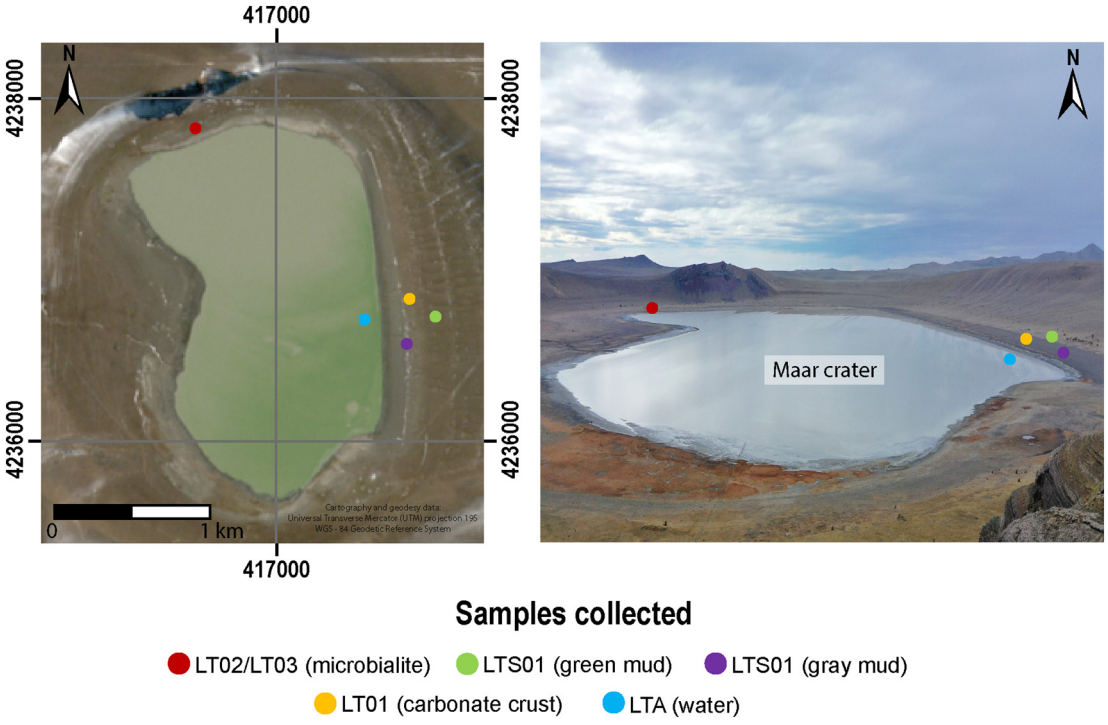

Fig. 2. Location of samples in study area.

BRAND® Titrette® digital bottle-top burette. To measure sodium and potassium, the flame emission method was performed using a Photometer model FC 280 from Celm. Gravimetry was used for total dissolved solids. The pH and conductivity were measured by potentiometry using sp2000 equipment Sensoglass brand. To geochemical simulations of the data, PHREEQC Interactive (Pfizer database) was used to calculate

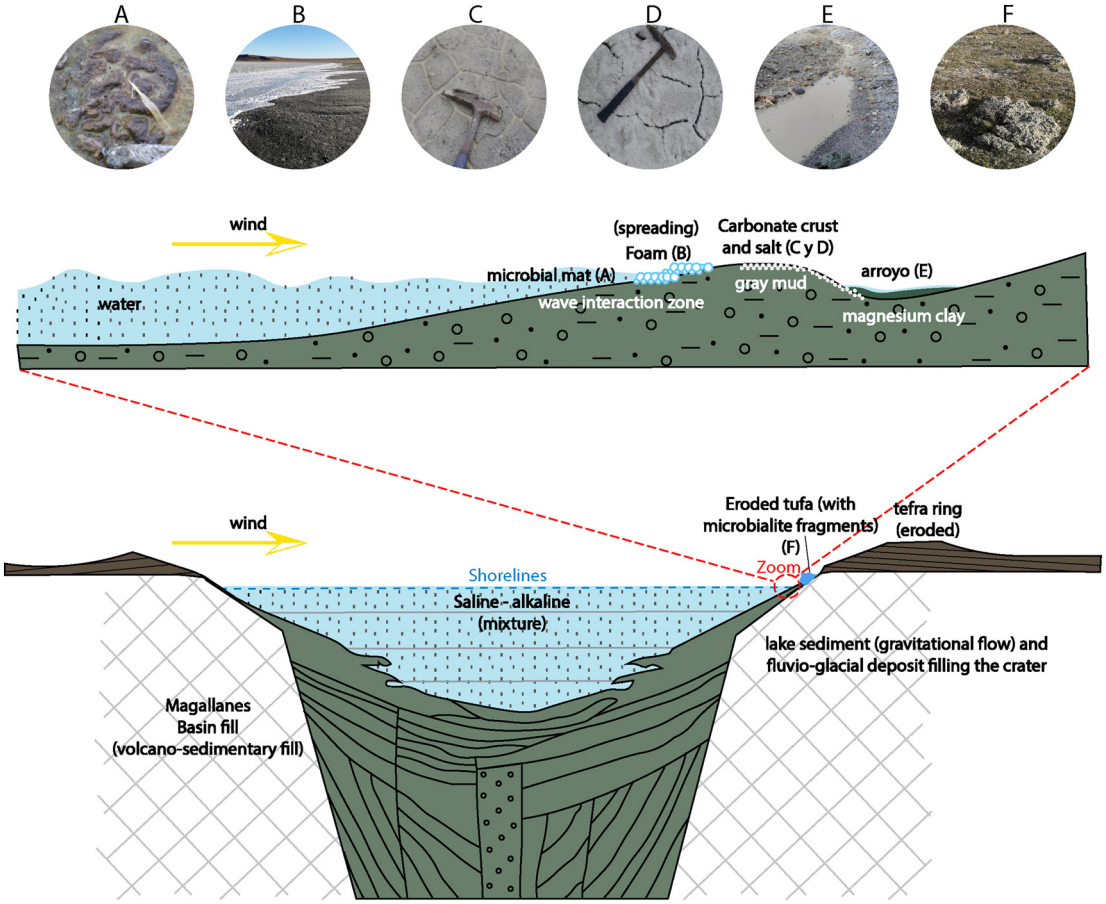

Fig. 3. Schematic model of Laguna Timone system.

Table 1
The image shows physicochemical characteristics of water sample. PHREEQC calculated (*) saturation states.

Physicochemical analysis of water	
	Water
Physical parameters	
Total dissolved solids (TDS) (mg/L)	110,576
pH	9.7
Electric conductivity (μS/cm)	111,000.00
Temperature (°C)	7
Chemical parameters (mg/L)	
Calcium (Ca)	9.00
Magnesium (Mg)	3.00
Sodium (Na)	29,076.00
Potassium (K)	2560.00
Iron (Fe)	0.42
Manganese (Mn)	0.25
Chloride (Cl)	41,000.00
Fluoride (F)	12.5
Sulfates (SO_2)	140
Phosphorus (PO_3)	110
Nitrates (NH_3)	358.15
Nitrites (NO_2)	0.272
Carbonates (CO_3)	29,997.43
Hydroxides (OH)	1018.32
Saturation states	
Ω calcite*	1.64
Ω aragonite*	1.8
Ω dolomite*	3.01

mineral saturation states. The supersaturation state (Ω) of a solution was calculated using a thermodynamic calculation as follows: $\Omega = ([Ca^{2+}]\ [CO_3^{2-}]\ /\ K^*_{sp})$ with ion activity product and K^*_{sp} the stoichiometric solubility product corresponding to the carbonate mineral (Stumm et al., 1996). In addition, the data was analyzed in the Piper diagram to classify the type of water.

5.2. Mineral and microstructure characterization of carbonates

The mineral and microfacies analyses of the microbialite fragments (Fig. 3) were performed using standard petrographic thin sections, examined under a Zeiss Image A2m microscope. The images were processed with the Axio Vision software. In addition, the morphology of carbonates was obtained using a JEOL model 6010LA scanning electron microscope equipped with detectors for secondary electrons, backscatter electrons, and the energy dispersive spectroscopy (EDS) model EX-94410T1L11 for images and operating equipment with a voltage of 20 kV and the magnification range of this instrument is 5× to 300,000×. Microtomography was used to visualize specific parts of an internal structure of carbonates, and it allows the observation of non-destructive cross-sections and three-dimensional parts. Computerized tomography produces an image closer to the real thing, for these thousand shares of radiographs of different rotation angles, from 0° to 360° (Cnudde et al., 2006). The previously selected rock samples were cut in a rectangular shape of approximately 1.0 cm × 3.0 cm. X-ray Microtomography, model 1172 from Skyscan, with 90 kV potential parameters, 112 μA current, and 12.8 8 μm/pixel resolution and computer "clusters" for analysis treatment and processing of results, allows microscale analysis. These analyses were performed at LAMIR Institute, housed at UFPR.

5.3. Chemical composition of carbonates and sediment

The X-ray diffraction (XRD) analyses of carbonate rocks and sediments (Fig. 3) were performed with the PANalytical X-ray diffractometer, model Empyrean with an X-Celerator detector, with CuKα radiation conditions with readings at a scan rate of 0.5°/min, under a voltage of 40 kV and current of 30 mA. The different carbonate minerals in the samples were determined from their *d*-spacing in the X-ray diffraction spectra following Zhang et al. (2010). The preparation of the samples for X-ray diffraction of the clay fraction was based on the manual of the procedures suggested by Kisch (1991), and clay mineral identifications were based on methods described through the comparison of peak positions and intensities in patterns obtained from treatments: air-dried, ethylene glycol and heating to 550 °C (Moore and Reynolds, 1997). The mineral composition was determined using the HighScore software at LAMIR Institute, housed at UFPR.

The quantitative chemical analysis by the X-ray fluorescence (XRF) method was used to identify and quantify the presence of 10 main oxides (SiO_2, $Al2O_3$, Fe_2O_3, CaO, MgO, K_2O, Na_2O, TiO_2, MnO, and P_2O_5) and trace elements (Sr, Ba, S, and Cl). The equipment used corresponds to the X-ray Fluorescence Spectrometer, from the PANalytical brand, model AXIOS mAX with a rhodium tube. The interpretation was conducted by the software SuperQ 5.3 at the LAMIR Institute, housed at UFPR.

The mineral and elemental mass of rocks and sediment were analyzed by an analytical technique known as automated mineralogical mapping by a TESCAN-TIMA instrument. Image analysis was performed simultaneously with SEM backscatter electron images combined with X-ray fluorescence. The operation is automated, and it has a robust database that transforms EDS chemical data to mineralogy. The equipment is housed in Chile at *Soluciones en microscopía y Mineralogía Aplicada* (SEMMA).

To obtain the morphological structure and chemical detail of the individual crystals and crystalline phases of clay fraction, the samples were pulverized and solubilized in 99.9 % alcohol and subsequently put in an ultrasound. To affix the particles a carbon film of 200 mesh - copper and later metalized was used. Images, qualitative analyses, and quantitative chemical analyses of clay fraction samples were obtained by a High-Resolution Transmission Electron Microscope – FEI TITAN G2, equipped at 300 kV at *Centro de Instrumentación Científica* (CIC), housed at the Universidad de Granada.

5.4. Isotope composition

A mass spectrometer model Delta V Advantage, brand Thermo Fischer Scientific, was used for the experimental acquisition of mineral C and O isotopic composition of microbialite fragments and crust (Fig. 3). The spectrometry is performed on CO_2 released from phosphoric acid digestion of carbonatic powder samples 'online' by reaction with 100 % H_3PO_4 at 72 °C using gas preparation and the introduction system Gas Bench II. Isotopic ratios were referenced in an international standard and are expressed in the 'δ' notation relative to Vienna Pee Dee Belemnite (VPDB). Data were processed by the software Isodat 3.0. These analyses were carried out at the LAMIR Institute, housed at UFPR.

6. Results

6.1. Water physiochemistry

6.1.1. Physico-chemical parameters (Table 1)

The lagoon water is cloudy and dirty. Physico-chemical parameters show that during May, the pH range is ca. 10, the electrical conductivity is 129,100 μS/cm, and dissolved solids are 67,100 ppm. The water temperature of the lake reaches a maximum of 1 °C. The water chemistry values correspond to Ca^{2+} (141.3 mg/L), Mg^{2+} (448 mg/l), chloride (18.785 mg/l), sodium (19,285 mg/l), potassium (856.9 mg/L), nitrate (229.3 mg/l), sulfate (727.1 mg/l) and phosphates (195.3 mg/l). During September the pH range is ca. 10, the electrical conductivity is 111,000 μS/cm, and dissolved solids are 110,567 ppm. The surficial water temperature of the lake reaches a maximum of 15 °C. The water chemistry shows Ca^{2+} (9 mg/L), Mg^{2+} (3 mg/l), and carbonate (29,997.43 mg/l). Comparing chloride (41,000 mg/l) ion average

results with different types of water, the concentrations are very high, even exceeding the average content in seawater. Sodium (29,076 mg/l), potassium (2560 mg/L), nitrate (358.15 mg/l), sulfate (140 mg/l) and phosphates (110 mg/l) follow.

Related to hydrochemical data, an analysis of the Piper diagram shows a strong tendency toward the sodium chloride type. Geochemical simulations to calculate mineral saturation states show that aragonite, calcite and dolomite could precipitate under the current physicochemical conditions of the lagoon. In this case, chemical analyses indicate that in both seasons the predominant mineral for the crust is calcite. The lake system indicates a temporal physical-chemistry variability between the months of May and September (Fig. 4). The Schoeller–Berkaloff diagram shows a chemical variation mainly for Ca^{2+} ion concentration.

6.2. Microstructural characterization of carbonates

The reworked nature of the tufa deposit with fragments of microbialites due to wind erosion and landslides coming from the surrounding volcanic rocks prevents a macroscopic facies characterization. However, features such as botroydal and spherulitic textures, and laminations are recognized at the microscopic scale. The samples from Laguna Timone are highly porous, have interparticle, vugs, and fenestral types. The porosity of carbonates could have been increased by weathering effects, fragmentation, and desiccation.

LT02 show the cloudy aspect due to the high content of organic material related to extracellular polymeric substances (EPS). It is possible to observe around a pebble clast as the material takes advantage of that substrate to start growing. This evidence is represented in macroscopic level where microbial mats are related with precipitated carbonates (Fig. 5A). Arborescent structures associated with coalescent oncoid with a micrite to microsparite matrix that varies between dark and light colors with irregular contours (Fig. 5B). The portions with massive texture (without porosity) are defined by intercalation of micrite and microsparite as layers with different tonalities, defining a millimeter crenulated internal lamination (Fig. 5C). Micro CT and SEM images show ramification with high porosity (53 %) (Fig. 5D) and few laminations with neo-crystal of calcite (Fig. 5E).

LT03 shows botryoidal structure defined by coalescent oncoid and a lumpy texture with a micrite, sparite, and microsparitic matrix. Small peloids are observed. Crystal aggregates tend to develop a subhedral and equant form. Intracrystalline microporosity, vuggy, and fenestral porosity are distinguishing (Fig. 6A). The oncoid isfilled with microcrystalline aggregates of calcite (Fig. 6B), showing concentric sheets around a nucleus. A spherical form is observed (Fig. 6C), and SEM shows similar forms of calcite (Fig. 6D). Micro CT images show nano-scale calcite crystals coalescing into spherical shapes, neo-forming calcite in botryoidal (Fig. 6E). The porosity is less than the LT02 sample (36 %) (Fig. 6F).

6.3. Chemical composition of carbonates

TESCAN-TIMA results reveal that mass percentage close to 100 % is calcite. Traces of anorthoclase, labradorite, quartz, amphibole, muscovite, and biotite are accessory minerals, probably as particles carried by the wind (Fig. 7A, B, C). In addition, the elemental analyses in the samples reveal Ca, C and O (Fig. 7D, E, F) as the main constituents,

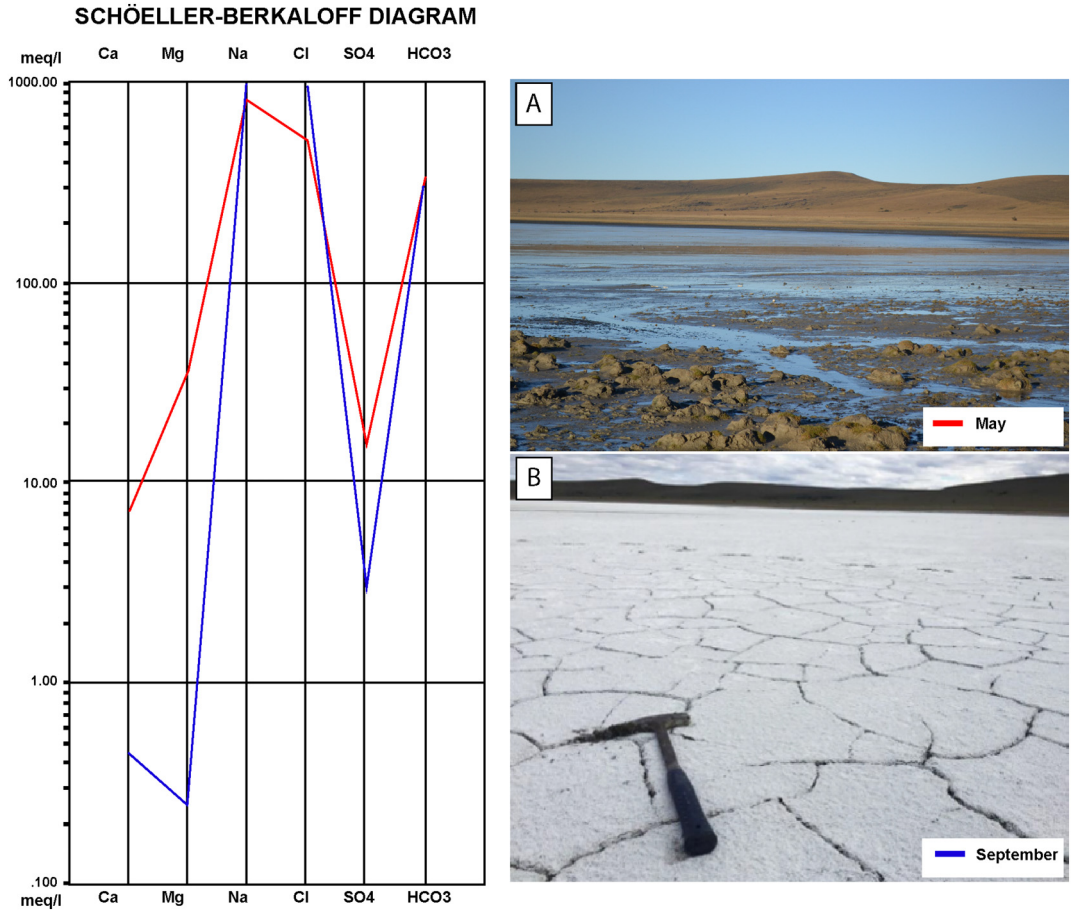

Fig. 4. The Schoeller–Berkaloff diagram shows the variation on ion concentration between May (2017) and September (2019) seasons. The red line represent May and blue line represent September. (For interpretation of the references to color in this figure legend, the reader is referred to the web version of this article.)

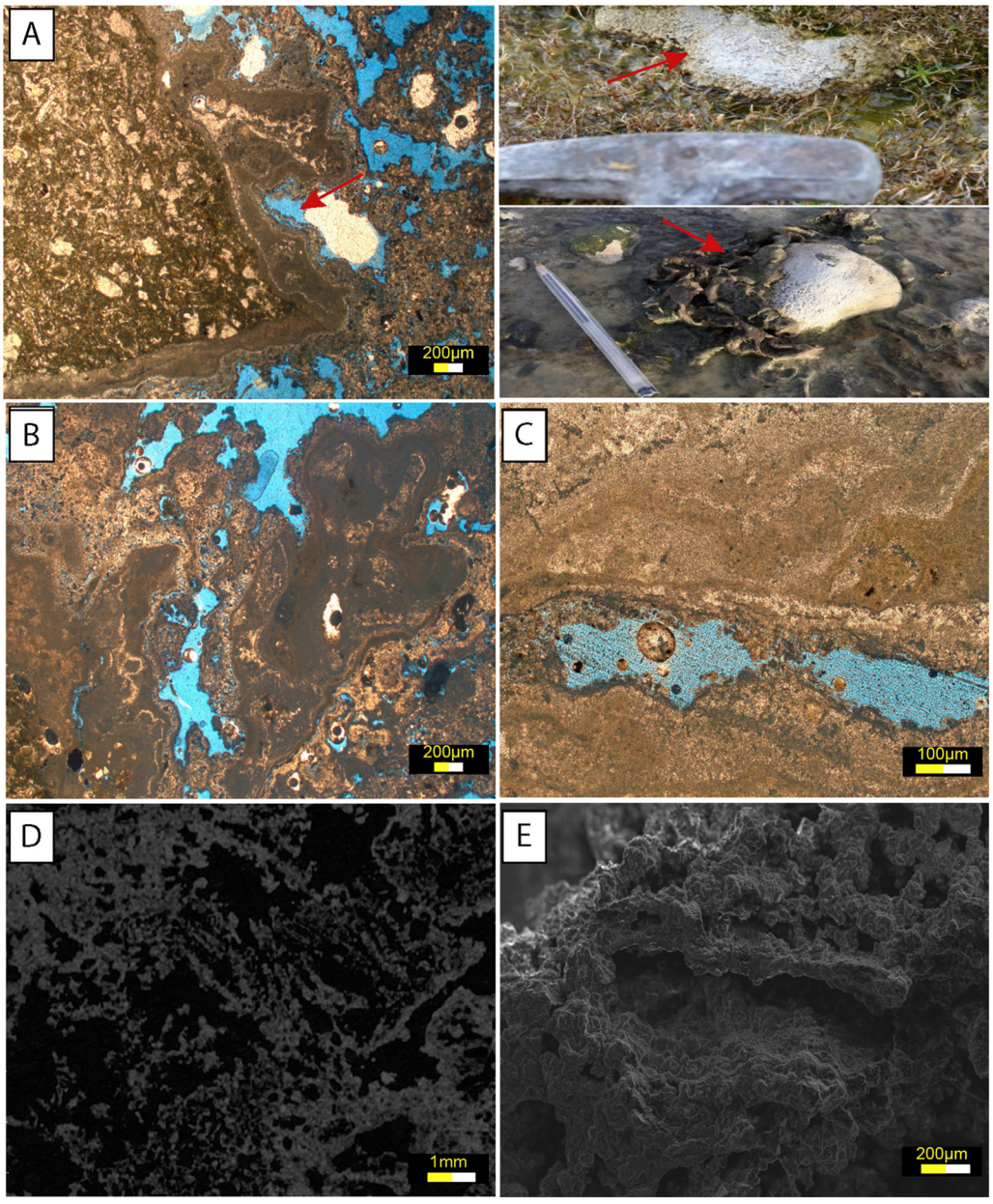

Fig. 5. A-The images show that carbonate precipitation takes advantage of that substrate (pebble) to start growing. Macroscopic observation linked microbial mats taking advantage of substrate to developed carbonate precipitated. B-Arborescent texture with a micrite to microsparite matrix, small peloids, and organic material. C-Massive texture, intercalation of micrite and microsparite with crenulated internal lamination. D-Micro CT image confirming a shrub-like form with high porosity; F-SEM imaging shows few laminations with neo-crystal of calcite.

with low magnesium content (>1 %), confirming that the carbonates correspond to calcite. Mineralogical XRD analysis verified the results delivered by TESCAN-TIMA and showed that all samples, crust (LT01) and microbialites (LT02, LT03) are mainly composed of calcite with a bit of variation in proportions among the samples. The classification of carbonate was based on the d-spacing values in X-ray diffraction spectra, following the evaluation from Zhang et al. (2010) showing calcite. (Table 2). Monohydrocalcite in the sample was detected in LT02, and fluorite is a trapped detrital mineral in carbonates LT01 and LT03.

6.4. C&O isotopy analysis

The carbon and oxygen isotopic ratios of samples of microbialite fragments and crust, were measured. The microbialite samples show an average isotopic composition for $\delta^{13}C$ of 1.82 $‰_{VPDB}$ and $\delta^{18}O$ a value of −5.94 $‰_{VPDB}$. It is possible to observe a clear difference in the isotopic composition of the carbonate crust showing a relative depletion of $\delta^{13}C$ with a value of −0.19 $‰_{VPDB}$ while for $\delta^{18}O$ it shows a considerable enrichment with a value of 2.0 $‰_{VPDB}$ (Fig. 8).

6.5. Chemical composition and microstructure of the clay minerals

TESCAN analysis showed chemical composition (%) of the following elements in the bulk sediments: O, Si, Ca^{2+}, Mg^{2+}, Fe, Al^{3+}, K+, Ti, C, Na^{+}, F^{-}, V, Mn, S, Cl, P, Cu, H, B, and REE (Fig. 9). It is only possible to observe a significant variation of Ca concentration between gray-mud (LTS01) and green-mud (LTS02), 6.97 % and 3.43 %, respectively. The lithological characteristics of the parental area are critical to justify the inputs of these elements, mainly Ca^{2+}, Mg^{2+} and Al^{3+} associated with mafic rocks. The source of Mg and Ca is related to weathering of

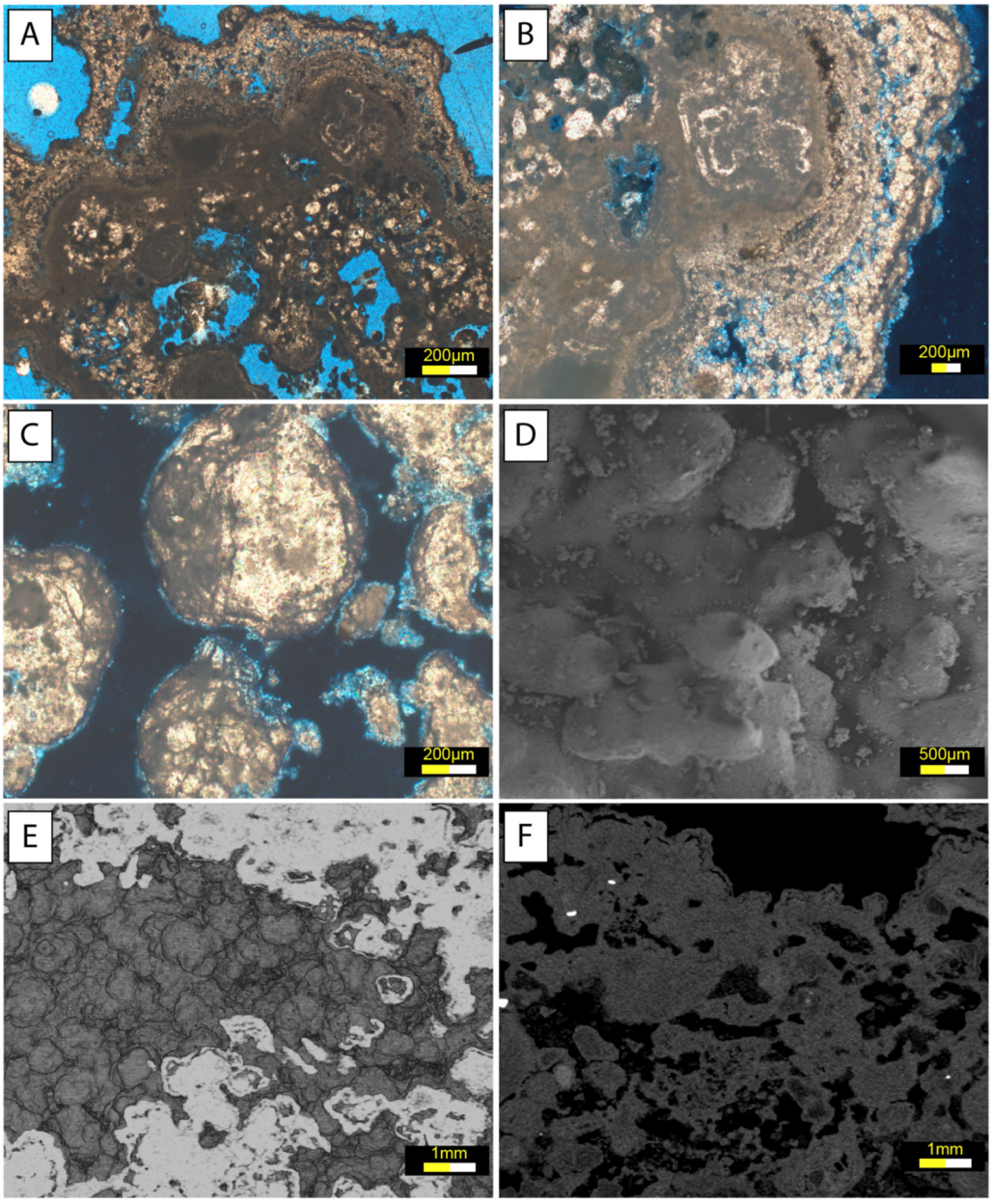

Fig. 6. A-Botryoidal structure showing coalescent oncoid and a lumpy texture with micrite, sparite and microsparitic matrix, small peloids, subhedral and equant crystal form. Intracrystalline microporosity, vuggy and fenestral porosity. B-Oncoid filled with microcrystalline aggregates of calcite showing concentric sheets around a nucleus associated. C, D-Spheroidal form. E, F-Micro CT images show nano-scale calcite crystals coalescing in spherical shapes.

minerals in basaltic rocks, such as olivine and orthopyroxene, and plagioclase and diopside, respectively. Regarding Si, glacial–fluvial deposits, clays, diatoms, detrital material, and weathering of the silicate's minerals may be possible sources.

The XRF analysis shows that major oxide content in gray-mud (sample LTS01) is characterized by high contents of SiO_2 (51.5 wt%) and CaO (17,2 wt%) followed by Al_2O_3 (9.3 wt%), Fe_2O_3 (7.8 wt%) MgO (5.3 wt%), Na_2O (3.5 wt%), K_2O (1,9 %) and Cl (1.1 %). The mass of the trace elements is below 1 wt%. The green-mud (sample LTS02) also indicates high contents of SiO_2 (51.5 wt%) but shows significant differences in Na_2O (17.9 wt%) and CaO (7.1 wt%) concentration in relation to the gray-mud. Al_2O_3 (9,3 wt%), Fe_2O_3 (8,0 wt%) and MgO (5.3 wt%) are similar. The Cl (7.7 wt%) and K_2O (3 wt%) concentration is notably higher. The mass of the trace elements (P, Mn, Sr, Ba, Rb, Br) is below 0.5 wt%. TiO_2 is less abundant (1 wt%) and can be considered as a minor constituent, but Ti has been used as an indicator for the presence of clay minerals (Koinig et al., 2003).

Several studies show that K is used as an indicator of clay (Kylander et al., 2011) associated with illite (Minyuk et al., 2007) related to K_2O, Na_2O, and CaO composition. The high Fe_2O_3 and MgO values in the sediments are indicators of chlorite related to Mg and Fe. These are two of the major elements of chlorite formation (Brownlow, 1996). Smectite is supported mainly by Si, Al, Mg, Ca, and Fe (Drief and Nieto, 2000).

Individual crystals cannot be identified in SEM images because the clay appears flaky, partially covering grains of detrital quartz and calcite. Therefore, the precise identification of the clay fraction was based on X-ray diffraction analyses, supported by TEM and EDX analyses showing the main elements involved. Clay mineral identifications were based on methods described by comparing peak positions and intensities in patterns obtained from treatments: air-dried, ethylene glycol, and heating to 550 °C (Moore and Reynolds, 1997).

Green mud (LTS02) (Fig. 10) showed a peak at 14.42 Å in air-dried conditions following treatment with ethylene glycol expanding to

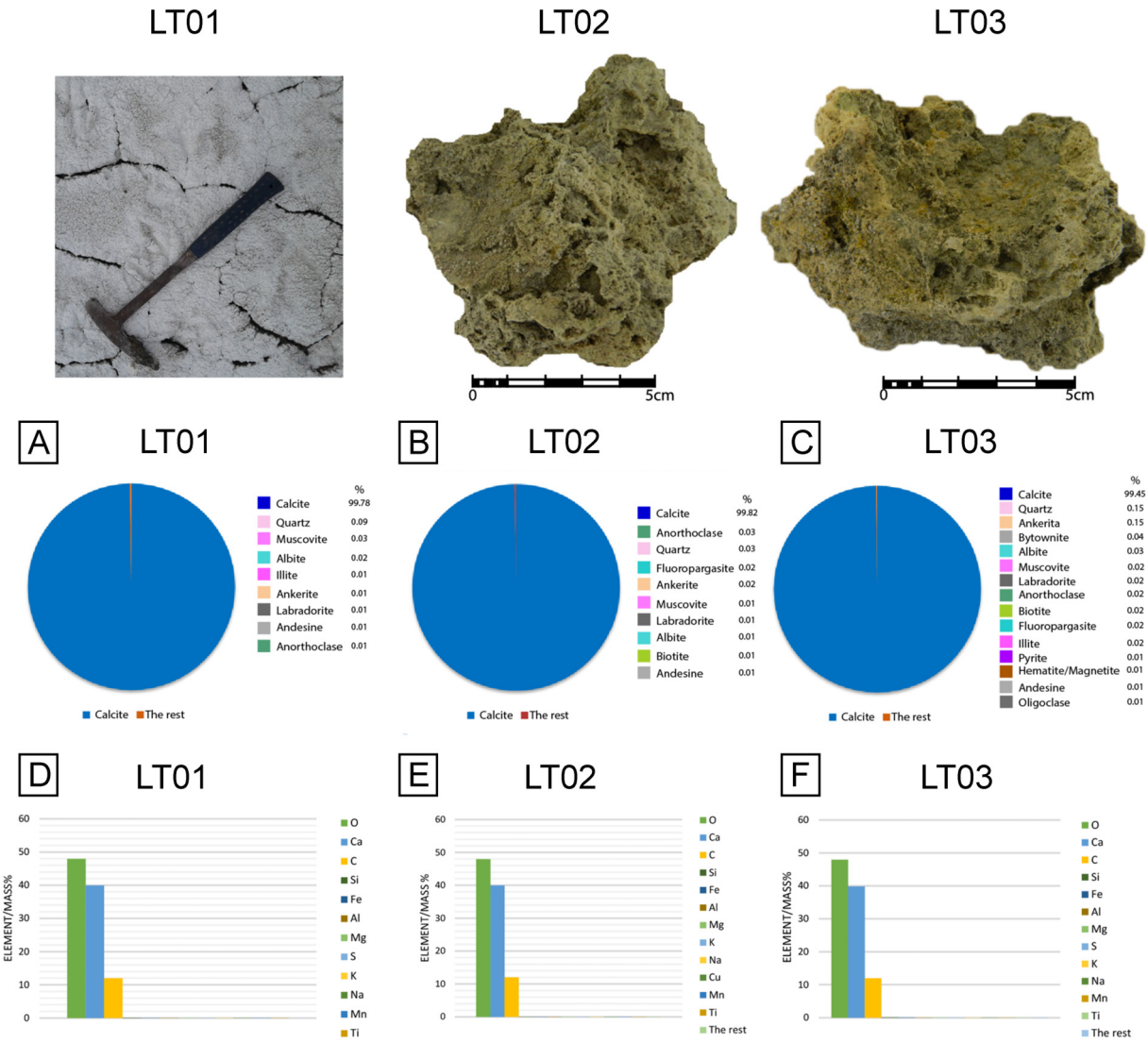

Fig. 7. TESCAN analyses of carbonates: A-Carbonate crust (LT01) composed by 99.78 % of calcite; B-LT02 composed by 99.85 % of calcite; C-LT03 composed by 99.45 % of calcite. All the samples contain detrital material <1 %.

17.55 Å through the 001 peaks and collapsing to 10.09 Å after heating to 550 °C, confirming the presence of a clay mineral of the smectite group (according to USGS-flow chart). Other clays identified in the samples correspond to members of the illite group characterized by intense 10.03 Å 001 peak and a 5.03 Å 002 peak unaltered by ethylene glycol and heating to 550 °C (Fanning et al., 1989).

Since the reflection at 7 Å corresponds to the sum between kaolinite (d_{001}) and chlorite (d_{002}), it is difficult to quantify them because they do not vary with the ethylene-glycol treatment and when they are heated to 550 °C the crystalline structure collapses. However, in this case, characteristic basal reflections of chlorite were represented by a 3.54 Å 004 peak. Therefore, in poly-mineral samples, a way to differentiate between kaolinite and chlorite is based on comparing the 3.58 Å kaolinite peak with the 3.54 Å chlorite peak (Biscaye, 1965), and the peak position of 7.10 Å indicates chlorite (Biscaye, 1964).

The quartz is identified by the intensity peaks corresponding to the reflections of 4.26 Å (d_{001}) and 3.35 Å (d_{002}) and 3.21 Å suggests the presence of feldspar. Gray-mud (LTS01) (Fig. 11) shows a difference in smectite peak absence. X-ray diffraction of the clay mineralogy of samples shows that smectite, chlorite, and illite to be the primary clay minerals, with quartz and potassium feldspar. Fig. 11 shows that the difference in intensity and crystallinity of smectite can be related to authigenic minerals.

Scanning electron microscopy (SEM images) shows mineral grains and an aggregate of fine crystals that generally have irregular morphologies. In some cases, spherical, angular, and tabular shapes were

Table 2
Mineralogical composition XRD and TESCAN-TIMA analysis.

Samples	XRD %	d (Å) carbonates	Mineral classification (Zhang et al., 2010)	Other mineral phases	TESCAN %	Mineral phases	Other mineral phases
LT03	89 %	3.03	Calcite	Fluorite	99.78 %	Calcite	Quartz, muscovite, plagioclase
LT01	98 %	3.03	Calcite	Monohydrocalcite	99.82 %	Calcite	Anorthoclase, quartz, fluorpargasite, ankerite
LT02	96 %	3.04	Calcite	Fluorite	99.45 %	Calcite	Quartz, ankerite, plagioclase

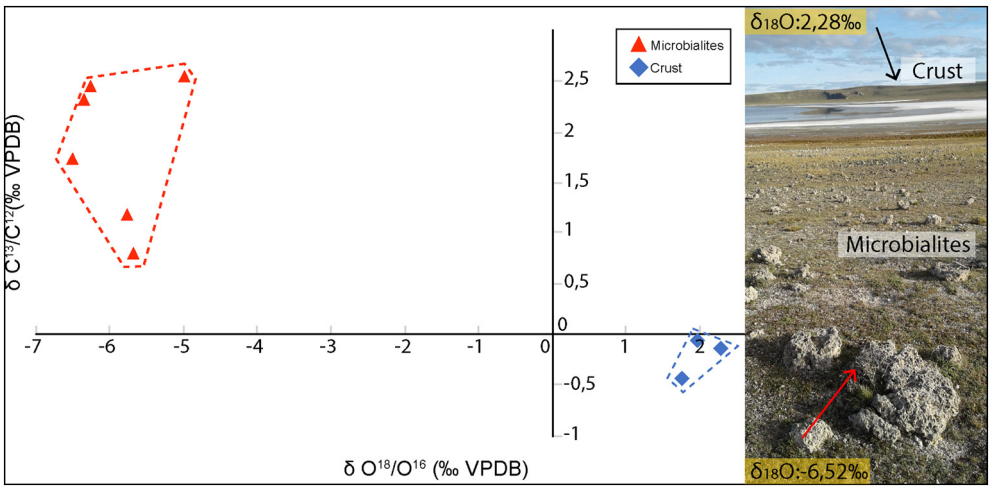

Fig. 8. Stable isotope data of oxygen and carbon of Laguna Timone samples.

identified. Within the mineral, grain calcite is dominated (Fig. 12A, B). In addition, a thin layer without defined morphology is covering the crystals (Fig. 12C). The EDX spectra of the different samples generally indicate a similar trend in terms of Si, Mg, Al, Na, Fe, Ca, and K in their composition (Fig. 12D). These characteristics are indicative of clay minerals. Also, the bulk sediment shows diatoms in the phase of dissolution inside (Fig. 12E).

Imaging obtained from Transmission electron microscopy (TEM) shows irregular morphologies like "cotton". Also, elongated crystals composed of Ca and O associated with calcite were identified (Fig. 12F, G). The "cotton" morphology is associated with authigenic processes and is common in smectites associated with reactive surfaces (Tosca, 2015; Tosca and Wright, 2015). Clay coatings on diatom structures (Fig. 12H) were observed. High-resolution TEM lattice-fringe images of the small clay particle show mixed-layer I–S packets of layer spacing from 1.3 nm characteristic of smectite and layer spacing from 1.0 nm characteristic of illite. The spacings correspond to the sum of illite and smectite-like layers (21.7–23 Å periodicity) (Fig. 12I) (Drits et al., 1997). Layers to 24 Å (Fig. 12J) are the result of an ordered sum of one chlorite layer (14 Å) and one contracted smectite layer

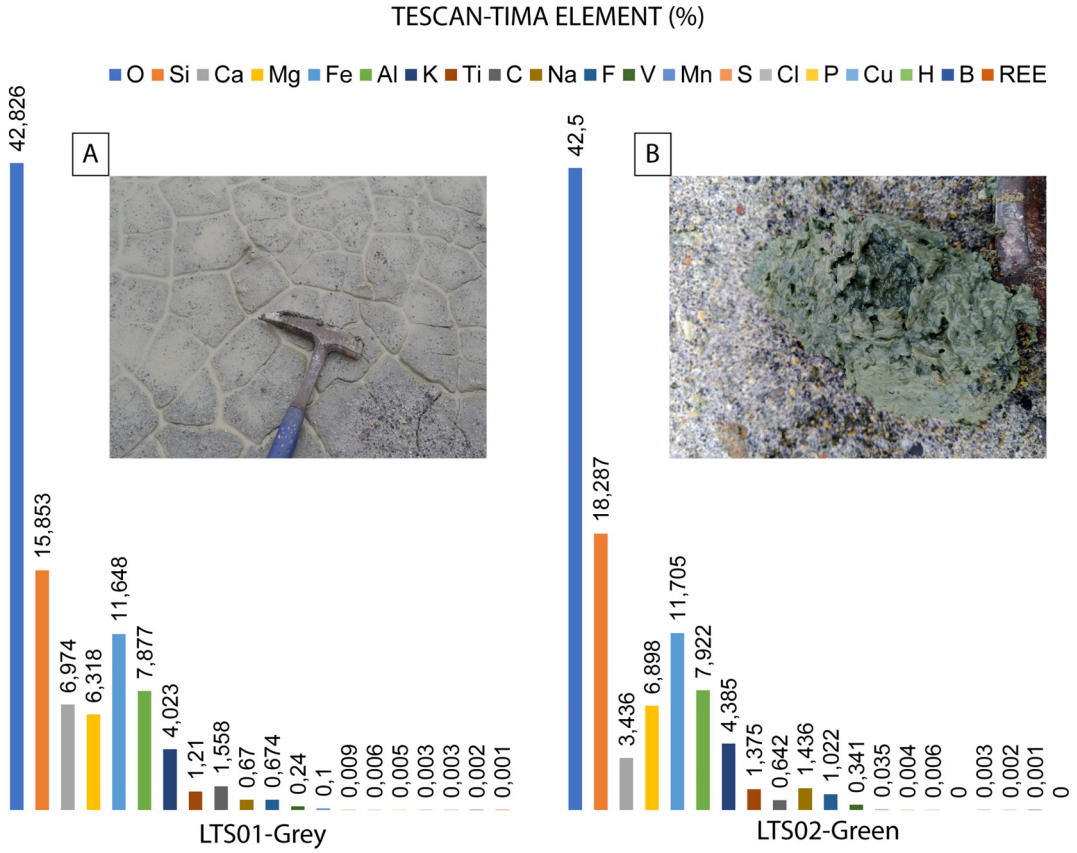

Fig. 9. Graphic shows elemental composition of the bulk sediments. A-Element concentration of gray-mud (LTS01). B-Element concentration of green-mud (LTS02).

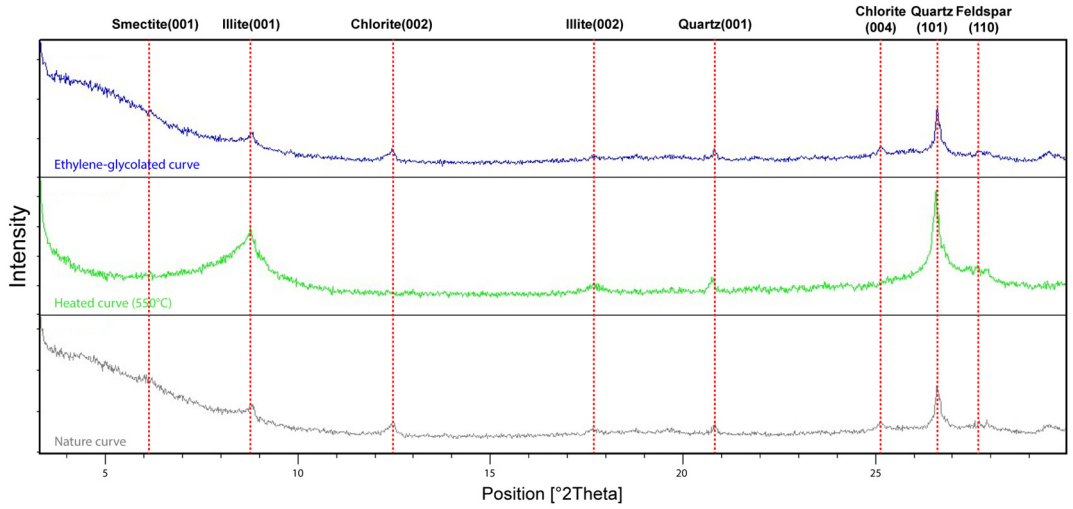

Fig. 10. XRD patterns of the clay fraction of green-mud (LTS02) sample of peak positions and intensities in patterns obtained from air-dried (AD), ethylene glycol (EG) and heating 550 °C (H) treatments. Smectite group was identified by AD: 14,42 Å, EG: 17,55 Å, H: 10,09 Å to 001 peak positions. Illite group was identified by AD: 10,03 Å, EG: 10,04 Å, H: 10,09 Å (d_{001}) and 5,03 Å (d_{002}). Chlorite group was identified by AD: 7,10 Å, EG: 7,10 Å, H: collapse (d_{002}) and 3.54 Å (d_{004}). The quartz is represented by 4,26 Å (d_{001}) and 3,35 Å (d_{002}) and 3,21 Å (d_{110}) suggest feldspar.

(10 Å) (Shau et al., 1990). TEM analysis shows that clay minerals correspond mainly to illite, smectite, and chlorite The mafic rock minerals such as pyroxene, olivine and plagioclase have been associated to the formation of illite, chlorite and smectite clay minerals in saline and arid environments (Needham et al., 2006; Dekayir et al., 2005; Wilson, 2004).

7. Discussions

7.1. Role of climatic/hydrochemical conditions

The cold waters of Laguna Timone are characterized by high salinity and alkalinity, being rich in calcium, magnesium, sodium, potassium, nitrate, nitrite, sulfate, and phosphates. The supersaturation state (Ω) calculated from the solution shows Ω (=1.64) is >1, indicating that is supersaturated with respect to $CaCO_3$ and thus suitable for carbonate precipitation. In this case associated to calcite, the high contents of chloride and sodium result in a high salinity in the lake system that exerted a key role in the increase of the solubility of minerals (O'Corner et al., 2001). The cations like Ca^{2+}, Mg^{2+}, and Fe^{2+}, and bicarbonate are released from the crystalline structure when exposed to saline solution increasing the alkalinity and pH of the aqueous system that subsequently favors the formation of carbonate minerals (Oelkers et al., 2015; Bundeleva et al., 2014; Dabirian et al., 2012; Kelemen et al., 2011; Ferris et al., 1994).

The lake is exposed under critical conditions, mainly extremely strong winds, low temperature and annual precipitation. The evaporation/precipitation processes are two critical factors that affect saline lakes (Williams, 2002). The strong winds at the latitudes of the PAVF are responsible for the permanent mix of the shallow water column and the high evaporation rates in the range of 1,000 to 1,600 mm/year (Ohlendorf et al., 2013; Mayr et al., 2007a). This process induces calcite supersaturation of water and leads to subsequent precipitation in Laguna Timone. Several lake-level fluctuations at Laguna Timone point to lake level variations triggered by prior hydrological changes. Changes in water level are evidenced by gradual withdrawal of the water in the crater, indicated by preserved paleo-shorelines which register a decrease in the water mass. On the other hand, the field observations show physical changes in the carbonate crust, and the Schoeller–Berkaloff diagram (Fig. 4) indicates chemical variations in ion concentrations. The result indicates the highest ion concentration (specifically Ca^{2+}) in the water when the extent of carbonate crust decreases around the lake. In this seasonal period, the temperature and wind are lower. In contrast, during periods of higher temperatures and strong winds the

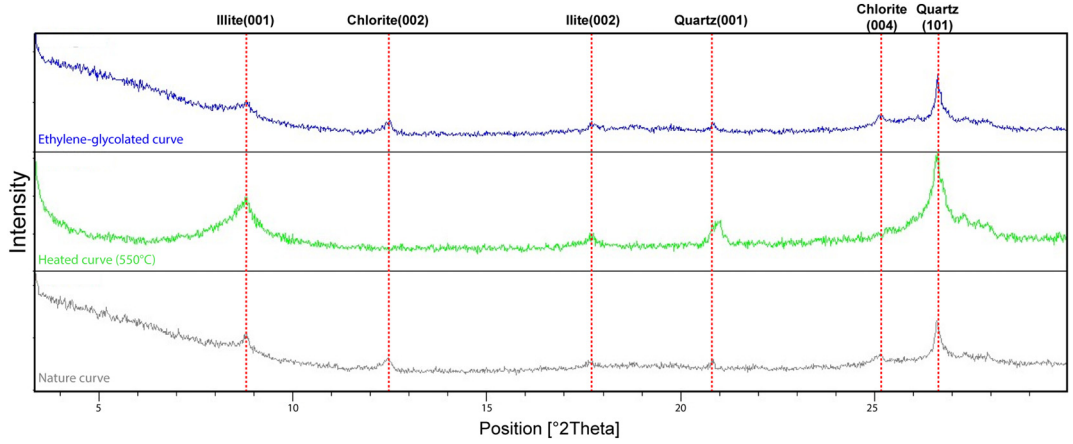

Fig. 11. XRD patterns of the clay fraction of gray-mud (LTS01) sample of peak positions and intensities in patterns obtained from air-dried, ethylene glycol and heating 550 °C treatments. Illite group was identified by AD: 10,04 Å, EG: 10,01 Å, H: 10,06 Å (d_{001}) and 5,03 Å (d_{002}). Chlorite group was identified by AD: 7,11 Å, EG: 7,09 Å, H: collapse to 002 and 3,54 Å 004 peak position. The quartz is represented by 4.26 Å (d_{001}) and 3,34 Å (d_{002}).

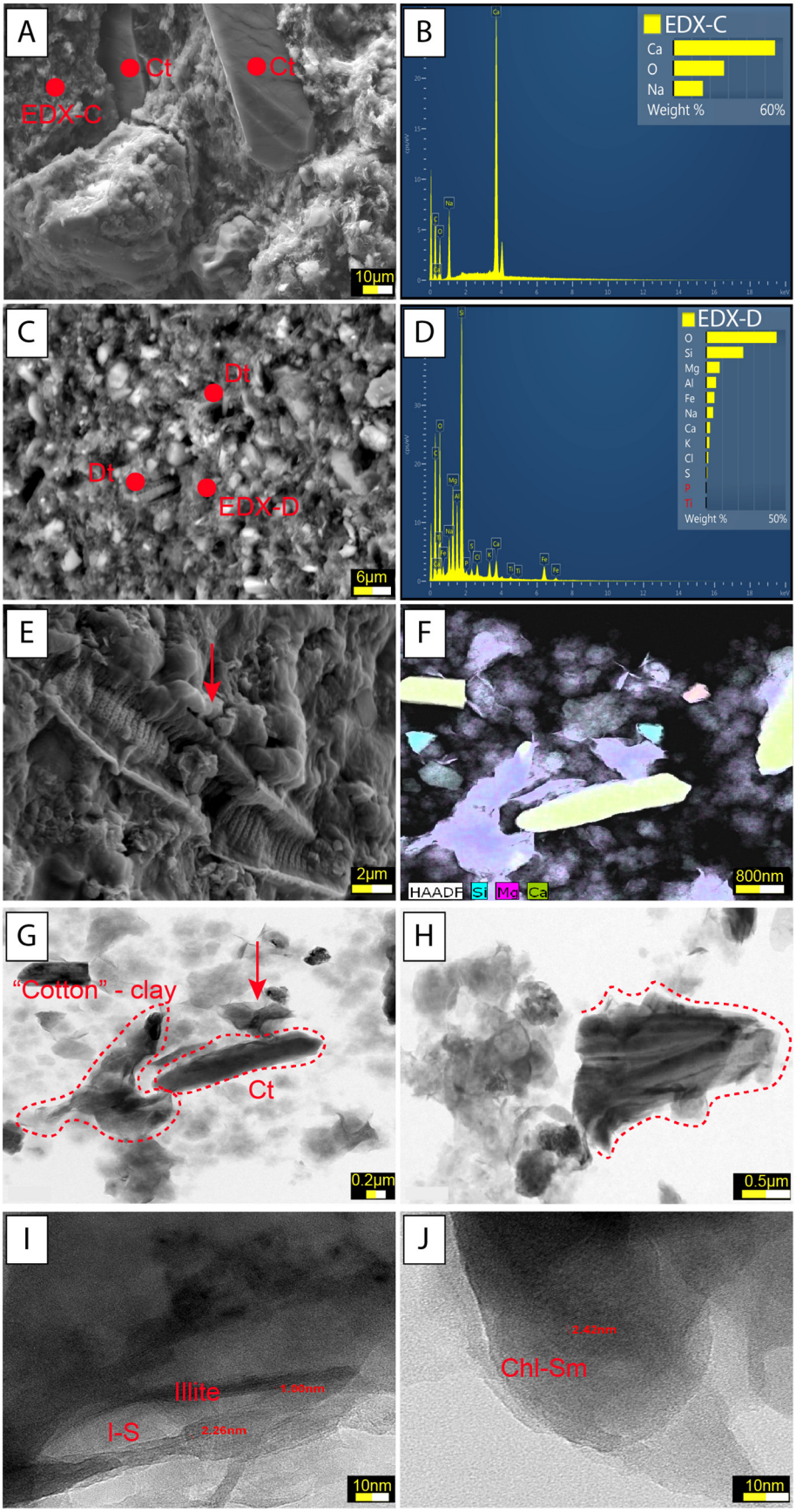
A
Ct
Ct
EDX-C
10µm
B
EDX-C
Ca
O
Na
Weight %
60%
C
Dt
Dt
EDX-D
6µm
D
EDX-D
O
Si
Mg
Al
Fe
Na
Ca
K
Cl
S
P
Ti
Weight %
50%
E
2µm
F
HAADF
Si
Mg
Ca
800nm
G
"Cotton" - clay
Ct
0.2µm
H
0.5µm
I
Illite
1.00nm
I-S
2.26nm
10nm
J
2.42nm
Chl-Sm
10nm

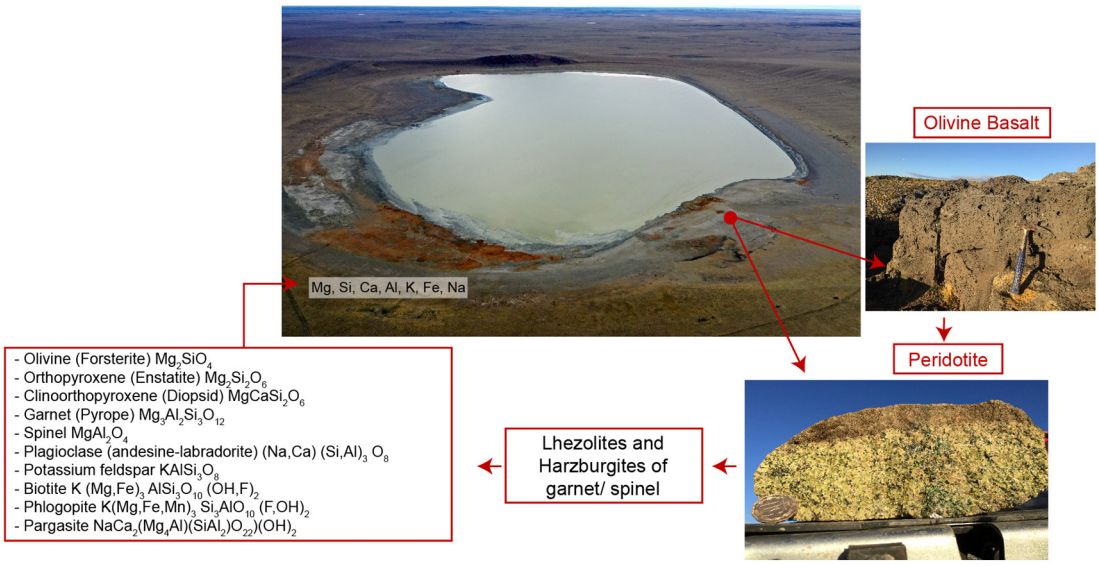

Fig. 13. Image shows the main source of availability elements in the system.

extent of carbonate precipitates increases. This fact results in a decrease of ion concentration in the lake, probably, associated to evaporative processes.

Isotope data show that positive $\delta^{18}O$ values (2.28 ‰) in carbonate crust are associated to evaporation processes. In contrast, the more negative $\delta^{18}O$ values (−6.52 ‰) observed in the microbialites possibly reflect fractionation produced by meteoric and/or groundwater influences. These data suggest that the microbialites level may have formed when the water level was higher, as recorded by the paleo-shoreline levels, corresponding to the oldest carbonate deposits, while the crust corresponds to modern deposits that register the current climatic variations (Fig. 8). The closed system of Laguna Timone inside an semi-arid environment is more susceptible for register climate and hydrochemical changes. The small variations were evidenced in the carbonates.

7.2. Implication of lithology in mineral precipitation

The weathering of silicates greatly impacts the soil formation and the cation release. The enriched chloride, sodium, fluoride, potassium, calcium, and magnesium compositions indicate that the chemical composition of superficial waters at Laguna Timone is influenced primarily by chemical weathering of bedrock minerals from mafic rocks and ultramafic components of the PAVF (Fig. 13). In the closed hydrological system of Laguna Timone, the composition of water is conditioned on the lithologies that are leached.

The physical and chemical disintegration of olivine, pyroxene, and plagioclase in basalts, and minerals in rare lherzolite and harzburgite xenoliths provides element availability as Ca, Mg, Fe, Al, Si, K, and Na and subsequently saturation of waters and sediment enrichment. The presence of olivine could be important in this context because studies show that the ion leaching from this mineral can drive the subsequent precipitation of carbonate related to their high weathering rates causing an important geochemical process on the carbon cycle (Olsson et al., 2012; White and Blum, 1995).

The clay fraction was characterized by illite, chlorite, and smectite. Several studies show that the weathering of mafic rocks can generated secondary mineralogy, such as interstratified/mixed-layer forms of smectite, corrensite, chlorite and illite (Needham et al., 2006; Dekayir et al., 2005; Wilson, 2004; Prudêncio et al., 2002; Drief et al., 2001; Singer, 1966). The Mg ion input from ferromagnesian minerals could lead to Mg-clay formation. The cotton-like morphologies associated with smectites by transformation and authigenic processes (Welton, 2003) from olivine, pyroxene chlorite and illite (Pozo and Calvo, 2018) were identified in Laguna Timone.

According to several studies, the occurrence of clays belonging to the smectite group is favored in evaporitic environments and semi-arid climatic conditions that are exposed to the contribution of ferromagnesian silicates and the alkaline and saline conditions promote the precipitation of these minerals (Pozo and Calvo, 2018; Calvo et al., 1999; Singer, 1984). Moreover, according to Tournassat et al. (2009), the clay minerals as smectites link hydrated Mg^{2+} within the interlaminar region stronger than ions as Na^+ and Ca^{2+}. Consequently, the cation exchange in smectite could reduce the inhibiting effect of Mg^{2+} on nucleation of $CaCO_3$ to favor the precipitation of calcite.

This evidence shows that the geological context is a conditioning factor on the formation of secondary minerals in the Laguna Timone system, where the external input is sporadic.

7.3. Microorganism–mineral relationship in carbonate precipitation

The authigenic clay precipitation requires a source of reactive silica. The data shows that reactive silica in Laguna Timone is supplied by diatoms, volcanic products and/or fluvioglacial deposits, and possibly unconsolidated pre-eruptive maar deposits exposed on the surface before phreatomagmatic eruptions (Zolitschka et al., 2006). The SEM images of sediment show partially dissolved diatoms. TEM analysis shows clay coatings on diatom structures. The Mg-clay is interrelated with calcite. This observation suggests that the calcite crystals may have formed from a Mg-clay gel that acts as an ideal substrate. The process could be mediate by microbial influence related to silica from dissolving diatoms. Diatoms produce EPS from binding of Fe, Al, Si, Ca, Mg, Na, K and other elements (Urbani et al., 2012; Underwood, 2010). In addition, some studies have reported that calcite can be precipitated

Fig. 12. Scanning electron microscope images. A-Thin sheet of clay minerals covering the elongate calcite crystals in gray-mud (LT01) sample. B-EDX analysis shows calcite. C-Thin sheet of clay minerals covering partially crystal and dissolved diatom in green-mud (LT02) sample. D-EDX analysis of thin sheet shows clay mineral composition of EDX point in C. E; F-Partially dissolved diatoms. G-"Cotton like" clays associated with Mg-clay and elongated crystal of calcite. H-Clay coatings on diatom structures. I-Thin packets of mixed-layer with spacings corresponding to the sum of illite- and smectite-like layer spacings (21–22 Å periodicity). J-Chlorite/smectite interstratification (24 Å periodicity).

from silicates rich in Si and Mg (Burne et al., 2014; Wright and Barnett, 2015; Bontognali et al., 2010; Dias et al., 2020).

Moreover, strong winds help the water to circulate through porosity and desiccation cracks favoring the dissolution of the diatom fragments enhanced by alkaline conditions.

On the other hand, cyanobacteria reported in the microbial mat of Laguna Timone (Henriquez, 2021) can influence Mg–Si substance precipitation through increases in pH producing undissociated H_4SiO_4 (Bischoff et al., 2020). Microscopic analysis and field images (Fig. 5) support the idea that the presence of microorganisms (EPS) has an influence on precipitation. Microbial influences increase the alkalinity in the system and likely play a role in the precipitation of $CaCO_3$. Photosynthetic organisms and extracellular polymeric substances (EPS) are the most important microbial processes in hypersaline lakes with microbial mats (Arp et al., 2012; Ludwig et al., 2005). The $\delta^{13}C$ (−0.43 ‰ to 2.50 ‰) values corroborate biotic and abiotic influences in carbonate precipitation of Laguna Timone.

8. Conclusions

The lakes of southern extra-Andean Patagonia are essential from a hydro-sedimentological perspective because they offer an opportunity to examine the genesis of a wide variety of chemical precipitates. This research reveals the interrelation of lithospheric, biological and atmospheric processes with carbonate precipitation that occur under exceptional conditions.

In this system, weathering of the mafic rocks, sporadic rain events, and sediment–groundwater interface provides the necessary element to saturate the system and leading to carbonate precipitation favored by strong winds and seasonal solar radiation that promote evaporative processes. On one hand, field observations and hydrochemical data show that the physical properties of carbonates are subject to climate changes. The isotope data show different precipitation processes between the crust and the microbialites. The crust records current variability in evaporation events. The microbialites associate their formation with an older record related to meteoric and/or groundwater sources.

On the other hand, calcite crystals are influenced by a Mg-clay gel that acts as an ideal substrate thought microbial influence related to silica from dissolving diatoms. The photosynthetic microorganisms affect the concentration of dissolved inorganic carbon increasing the pH of an environment generating the necessary conditions to precipitate carbonate. The $\delta^{13}C$ values indicate that the carbonate precipitation is controlled by either physicochemical and/or biochemical processes. The intense interaction between volcanic, biological, hydrological and glacial processes makes southern South America one of the most interesting places to investigate and register the behavior of the climate system over time.

Declaration of competing interest

The authors declare that they have no known competing financial interests or personal relationships that could have appeared to influence the work reported in this paper.

Acknowledgments

To Mirko Zec and Graciela Soto for their hospitality and support during the fieldwork carried out at the Estancia La Portada. We also thank Daniel Patias, Veleda Muller, Isis Armstrong, Gustavo Marangon, Sergio Carvajal, Gustavo Barrientos, Valeria Banda, Vicente Amand de Mendieta, Paulo Quezada, Daniela Plá, and M. Cristina Silva, who participated in different fieldwork campaigns. Chemists and technicians from the LAMIR Institute for their general help in the laboratory. We also thank Francisca Martinez from Granada University for support with clay mineral analysis. We also thank the Diagenesis Project (ANP 20257/2). ANP (Agência Nacional de Petróleo, Gás Natural e Biocombustíveis), Shell Brasil Petróleo LTDA. Fondecyt project 1211906 (M.C.), Chile.

References

Arp, G., Helms, G., Karlinska, K., Schumann, G., Reimer, A., Reitner, J., Trichet, J., 2012. Photosynthesis versus exopolymer degradation in the formation of microbialites on the atoll of Kiritimati, Republic of Kiribati, Central Pacific. Geomicrobiology Journal 29, 29–65. https://doi.org/10.1080/01490451.2010.521436.

Barros, V., Scian, B., Mattio, H., 1979. Campos de precipitación de la provincia de Chubut (1931–1960). Geoacta 10, 175–192.

Biscaye, P.E., 1964. Distinction between kaolinite and chlorite in recent sediments by X-ray diffraction. American Mineralogist 49, 1281–1289.

Biscaye, P.E., 1965. Mineralogy and sedimentation of recent deep-sea clay in the Atlantic Ocean and adjacent seas and oceans. Geological Society of America Bulletin 76, 803–832.

Bischoff, K., Sirantoine, E., Wilson, M.E., George, A.D., Mendes Monteiro, J., Saunders, M., 2020. Spherulitic microbialites from modern hypersaline lakes, Rottnest Island, Western Australia. Geobiology 18, 725–741. https://doi.org/10.1111/gbi.12400.

Bockheim, J., Coronato, A., Rabassa, J., Ercolano, B., Ponce, J., 2009. Relict sand wedges in southern Patagonia and their stratigraphic and paleo-environmental significance. Quaternary Science Reviews 28, 1188–1199. https://doi.org/10.1016/j.gloplacha.2012.10.018.

Bontognali, T.R.R., Vasconcelos, C., Warthmann, R.J., Bernasconi, S.M., Dupraz, C., Strohmenger, C.J., Mckenzie, J.A., 2010. Dolomite formation within microbial mats in the coastal sabkha of Abu Dhabi (United Arab Emirates). Sedimentology 57, 824–844. https://doi.org/10.1111/j.1365-3091.2009.01121.x.

Brownlow, A.H., 1996. Geochemistry. second ed. Prentice Hall, Upper Saddle River, New Jersey (580 pp.).

Bundeleva, I.A., Shirokova, L.S., Pokrovsky, O.S., Bénézeth, P., Ménez, B., Gérard, E., Balor, S., 2014. Experimental modeling of calcium carbonate precipitation by cyanobacterium Gloeocapsa sp. Chemical Geology 374, 44–60. https://doi.org/10.1016/j.chemgeo.2014.03.007.

Burne, R.V., Moore, L.S., Christy, A.G., Troitzsch, U., King, P.L., Carnerup, A.M., Hamilton, P.J., 2014. Stevensite in the modern thrombolites of Lake Clifton, Western Australia: a missing link in microbialite mineralization? Geology 42, 575–578. https://doi.org/10.1130/G35484.1.

Calderón, M., Fildani, A., Herve, F., Fanning, C.M., Weislogel, A., Cordani, U., 2007. Late Jurassic bimodal magmatism in the northern sea-floor remnant of the Rocas Verdes basin, southern Patagonian Andes. Journal of the Geological Society of London 162, 1011–1022. https://doi.org/10.1144/0016-76492006-102.

Calvo, J.P., Blanc-Valleron, M.M., Rodríguez-Aranda, J.P., Rouchy, J.M., Sanz, M.E., 1999. Authigenic clay minerals in continental evaporitic environments. In: Thiry, M., Simon-Coinçon, R. (Eds.), Palaeoweathering, Palaeosurfaces and Related Continental Deposits. Special Publications of the International Association of Sedimentologists, Oxford, pp. 129–155.

Cnudde, V., Marcelino, V., Masschaele, B., Vlassenbroeck, J., Dierick, M., Van Hoorebeke, L., Jacobs, P., 2006. Non-destructive high-resolution X-ray CT as an aid for the quantification of soil compaction. Geophysical Research Abstracts v8.

Corbella, H., 2002. El campo volcano-tectónico de Pali Aike. Geología y Recursos Naturales de Santa Cruz, Buenos Aires. Asociación Geológica Argentina, pp. 285–302.

Corbella, H., Gagliardini, D., 1997. Caracterización morfológica de la faja volcano tectónica "Pali Aike" mediante imagenes ERS-1. Proceeding of an International Seminar on the Use and Applications of ERS in Latin America, Viña del Mar, Chile.

Corbella, H., Chelotti, L., Pomposiello, C., 1996. Neotectonica del rift Jurasico austral en Pali Aike, Patagonia Extrandina, Santa Cruz, Argentina. XIII Congreso Geológico Argentino y III Congreso de Exploración de Hidrocarburos, Buenos Aires, Actas VII, pp. 383–393.

Coronato, A., Rabassa, J., 2011. Pleistocene glaciations in southern Patagonia and Tierra del Fuego. In: Ehlers, J., Gibbard, P. (Eds.), Quaternary Glaciations e Extent and Chronology, Part IV e A Closer Look. Elsevier Developments in Quaternary Sciencevol. 15, pp. 715–727.

Dabirian, R., Beiranvand, M., Aghahoseini, S., 2012. Mineral carbonation in peridotite rock for CO2 sequestration and a method of leakage reduction of CO2 in the rock. Nafta 63, 44–48.

Dekayir, A., Amouric, M., Olives, J., 2005. Clay minerals in hydrothermally altered basalts from Middle Atlas, Morocco. Clay Minerals 40, 67–77. https://doi.org/10.1180/0009855054010156.

Dias, I.A., Cury, L.F., Titon, B.G., Athayde, G.B., Fedalto, G., da Rocha Santos, L., Manuela Bahniuk Rumbeslperger, A., 2020. The occurrence of authigenic clay minerals in alkaline-saline lakes, Pantanal Wetland (Nhecolândia Region, Brazil). Minerals 10, 718. https://doi.org/10.3390/min10080718.

Dickinson, W.R., Snyder, W.S., 1979. Geometry of subducted slabs related to San Andreas transform. Journal of Geology 87, 609–627.

Diraison, M., Cobbold, P., Gapais, D., Rossello, E., 1997. Magellan Strait: part of the Neogene rift system. Geology 25, 703–706.

D'Orazio, M., Agostini, S., Mazzarini, F., Innocenti, F., Manetti, P., Haller, M.J., Lahsen, A., 2000. The Pali Aike volcanic field, Patagonia: slab-window magmatism near the tip of South America. Tectonophysics 321, 407–427. https://doi.org/10.1016/S0040-1951(00)00082-2.

D'orazio, M., Agostini, S., Innocenti, F., Manetti, P., Haller, M., Mazzarini, F., 2001. Slab-window related magmatism from the southernmost South America: the Late Miocene mafic volcanics from the Estancia Glencross Area (~52°S, Argentina–Chile). Lithos 57, 67–89.

Drief, A., Nieto, E., 2000. Chemical composition of smectites formed in clastic sediments. Implications for the smectite–illite transformation. Clay Minerals 35, 665–678. https://doi.org/10.1180/000985500547124.
Drief, A., Nieto, F., Sanchez-Navas, A., 2001. Experimental clay-mineral formation from a subvolcanic rock by interaction with 1M NaOH solution at room temperature. Clays and Clay Minerals 49, 92–106. https://doi.org/10.1346/CCMN.2001.0490108.
Drits, V.A., Lindgreen, H., Sakharov, B.A., Salyn, A.S., 1997. Sequential structure transformation of illite–smectite–vermiculite during diagenesis of Upper Jurassic shales, North Sea. Clay Minerals 33, 351–371. https://doi.org/10.1180/claymin.1997.032.3.03.
Fanning, D.S., Keramidas, V.Z., El-Desoky, M.A., 1989. Micas. Minerals in Soil Environments 1, 551–634.
Ferris, F.G., Wiese, R.G., Fyfe, W., 1994. Precipitation of carbonate minerals by microorganisms: Implications for silicate weathering and the global carbon dioxide budget. Geomicrobiology Journal 12, 1–13. https://doi.org/10.1080/01490459409377966.
Fosdick, J.C., Romans, B.W., Fildani, A., Bernhardt, A., Calderón, M., Graham, S.A., 2011. Kinematic evolution of the Patagonian retro-arc fold-and-thrust belt and Magallanes foreland basin, Chile and Argentina, 51°30′S. Geological Society of America Bulletin 123, 1679–1698. https://doi.org/10.1130/B30242.1.
Garreaud, R., Lopez, P., Minvielle, M., Rojas, M., 2013. Large-scale control on the Patagonian climate. Journal of Climate 26, 215–230. https://doi.org/10.1175/JCLI-D-12-00001.1.
Henriquez, C., 2021. Understanding the Precipitation Processes of Carbonate Deposits Relate to the Postmagmatic History of Laguna Timone, Pali Aike Volcanic Field, Chilean Extra-Andean. Universidade Federal do Paraná, Curitiba, Brazil (M.D. Thesis).
Herve, F., Pankhurst, R.J., Fanning, C.M., Calderon, M., Yaxley, G.M., 2007. The South Patagonian batholith: 150 my of granite magmatism on a plate margin. Lithos 97, 373–394. https://doi.org/10.1016/j.lithos.2007.01.007.
Kelemen, P.B., Matter, J., Streit, E.E., Rudge, J.F., Curry, W.B., Blusztajn, J., 2011. Rates and mechanisms of mineral carbonation in peridotite: natural processes and recipes for enhanced, in situ CO_2 capture and storage. Annual Review of Earth and Planetary Sciences 39, 545–576. https://doi.org/10.1146/annurev-earth-092010-152509.
Kisch, J., 1991. Calibration of the anchizone a critical comparison of illite 'cristallinity' scales used for definition. Journal of Metamorphic Geology 8, 31–46. https://doi.org/10.1111/j.1525-1314.1990.tb00455.x.
Koinig, K.A., Shotyk, W., Lotter, A.F., Ohlendorf, C., Sturm, M., 2003. 9000 years of geochemical evolution of lithogenic major and trace elements in the sediment of an alpine lake—the role of climate, vegetation, and landuse history. Journal of Paleolimnology 30, 307–320. https://doi.org/10.1023/A:1026080712312.
Kylander, M.E., Ampel, L., Wohlfarth, B., Veres, D., 2011. Highresolution X-ray fluorescene core scanning analysis of Les Echets (France) sedimentary sequence: new insights from chemical proxies. Journal of Quaternary Science 26, 109–117. https://doi.org/10.1002/jqs.1438.
Lagarrigue, S., Elgueta, S., Arancibia, G., Sanchez, J., Morata, D., Rojas, L., 2019. The Springhill Formation (Jurassic-Cretaceous) as a potential low enthalpy geothermal reservoir in the Cerro Sombrero area, Magellan Basin, Chile. Geophysical Research Abstracts 21.
Ludwig, R., Al-Horani, F.A., De Beer, D., Jonkers, H.M., 2005. Photosynthesis- controlled calcification in a hypersaline microbial mat. Journal of Limnology and Oceanography 50, 1836–1843. https://doi.org/10.4319/lo.2005.50.6.1836.
Mayr, C., Lücke, A., Stichler, W., Trimborn, P., Ercolano, B., Oliva, G., Ohlendorf, C., Soto, J., Fey, M., Haberzettl, T., Janssen, S., 2007a. Precipitation origin and evaporation of lakes in semi-arid Patagonia (Argentina) inferred from stable isotopes (δ18O, δ2H). Journal of Hydrology 334, 53–63. https://doi.org/10.1016/j.jhydrol.2006.09.025.
Mayr, C., Wille, M., Haberzettl, T., Fey, M., Janssen, S., Lücke, A., Ohlendorf, C., Oliva, G., Schäbitz, F., Schleser, G.H., Zolitschka, B., 2007b. Holocene variability of the Southern Hemisphere westerlies in Argentinean Patagonia (52 S). Quaternary Science Reviews 26, 579–584. https://doi.org/10.1016/j.quascirev.2006.11.013.
Mazzarini, F., D'Orazio, M., 2003. Spatial distribution of cones and satellite-detected lineaments in the Pali Aike Volcanic Field (southernmost Patagonia): insights into tectonic setting of a Neogene rift system. Journal of Volcanology and Geothermal Research 125, 291–305. https://doi.org/10.1016/S0377-0273(03)00120-3.
Mella, P., 2001. Control tectónico en la evolución de la cuenca de antepaís de Magallanes, XII Región, Chile. Memoria para optar al título de geólogo, Universidad de Concepción, Facultad de Ciencias Químicas, p. 143.
Minyuk, P., Brigham-Grette, J., Melles, M., Borkhodoev, V.Y., Glushkova, O.Y., 2007. Inorganic geochemistry of El gygytgyn Lake sediments, northeastern Russia, as an indicator of paleoclimatic change for the last 250 kyr. Journal of Paleolimnology 37, 123–133.
Moore, D.M., Reynolds, J.R.R.C., 1997. X-ray Diffraction and the Identification and Analysis of Clay Minerals. 2nd edition. Oxford University Press, New York.
Needham, S.J., Worden, R.H., Cuadros, J., 2006. Sediment ingestion by worms and the production of bio-clays: a study of macrobiologically enhanced weathering and early diagenetic processes. Sedimentology 53, 567–579. https://doi.org/10.1111/j.1365-3091.2006.00781.x.
O'Corner, W.K., Dahlin, D.C., Nilson, D.N., Rush, G.E., Gerdemann, S.J., Walters, R.P., Turner, R.C., 2001. Aqueous Mineral Carbonation Studies Using Olivine and Sepertine. Albany Research Center.
Oelkers, E.H., Benning, L.G., Lutz, S., Mavromatis, V., Pearce, C.R., Plumper, O., 2015. The efficient long-term inhibition of forsterite dissolution by common soil bacteria and fungi at Earth surface conditions. Geochimica et Cosmochimica Acta 168, 222–235.
Ohlendorf, C., Fey, M., Gebhardt, C., Haberzettl, T., Lücke, A., Mayr, C., Schäbitz, F., Wille, M., Zolitschka, B., 2013. Mechanisms of lake-level change at Laguna Potrok Aike (Argentina)–insights from hydrological balance calculations. Quaternary Science Reviews 71, 27–45.
Olsson, J., Bovet, N., Makovicky, E., Bechgaard, K., Balogh, Z., Stipp, S.L.S., 2012. Olivine reactivity with CO2 and H2O on a microscale: implications for carbon sequestration. Geochimica et Cosmochimica Acta 77, 86–97. https://doi.org/10.1016/j.gca.2011.11.001.
Pozo, M., Calvo, J.P., 2018. An overview of authigenic magnesian clays. Minerals 8, 520. https://doi.org/10.3390/min8110520.
Prudêncio, M.I., SequeiraBraga, M.A., Paquet, H., Waerenborgh, J.C., Pereira, L.C.J., Gouveia, M.A., 2002. Clay mineral assemblages in weathered basalt profiles from central and southern Portugal: climatic significance. Catena 49, 77–89. https://doi.org/10.1016/S0341-8162(02)00018-8.
Rabassa, J., Coronato, A.M., Salemme, M., 2005. Chronology of the Late Cenozoic Patagonian glaciations and their correlation with biostratigraphic units of the Pampean region (Argentina). Journal of South American Earth Sciences 20, 81–103. https://doi.org/10.1016/j.jsames.2005.07.004.
Ross, P.-S., Delpit, S., Haller, M.J., Németh, K., Corbella, H., 2011. Influence of the substrate on maar diatreme volcanoes – an example of a mixed setting from the Pali Aike volcanic field, Argentina. Journal of Volcanology and Geothermal Research 201, 253–271. https://doi.org/10.1016/j.jvolgeores.2010.07.018.
Shau, Y.H., Peacor, D.R., Essene, E.J., 1990. Corrensite and mixed-layer chlorite/smectite in metabasalt from northern Taiwan: TEM/AEM, EMPA, XRD, and optical studies. Contributions to Mineralogy and Petrology 105, 123–142. https://doi.org/10.1007/BF00678980.
Singer, A., 1966. The mineralogy of the clay fraction from basaltic soils in the Galilee, Israel. Journal of Soil Science 17, 136–147. https://doi.org/10.1111/j.1365-2389.1966.tb01461.x.
Singer, A., 1984. Pedogenic palygorskite in the arid environment. In: Singer, A., Galán, E. (Eds.), Palygorskite-Sepiolite. Occurrences, Genesis and Uses. Developments in Sedimentology. Elsevier, Amsterdam, The Netherlands, pp. 169–177.
Skewes, M.A., Stern, C.R., 1979. Petrology and geochemistry of alkali basalts and ultramafic inclusions from the Palei-Aike volcanic field in southern Chile and the origin of the Patagonian plateau lavas. Journal of Volcanology and Geothermal Research 6, 3–25. https://doi.org/10.1016/0377-0273(79)90044-1.
Stumm, W., Morgan, J.J., Drever, J.I., 1996. Aquatic chemistry. Journal of Environmental Quality 25, 1162.
Ton-That, T., Singer, B., Mörner, N.A., Rabassa, J., 1999. Datación de lavas basálticas por 40Ar/39Ar y geología glacial de la región del lago Buenos Aires, provincia de Santa Cruz, Argentina. Revista de la Asociación Geológica Argentina 54, 333–352.
Tosca, N.J., 2015. Geochemical pathways to Mg-clay formation. In: Pozo, M., Galán, E. (Eds.), Magnesian Clays: Characterization, Origins and Applications. AIPEA (Association Internationale pour l'Etude des Argiles), pp. 283–329.
Tosca, N.J., Wright, V.P., 2015. Diagenetic pathways linked to labile Mg-clays in lacustrine carbonate reservoirs: a model for the origin of secondary porosity in the Cretaceous pre-salt Barra Velha Formation, offshore Brazil. Geological Society of London 435, 33–46. https://doi.org/10.1144/SP435.1.
Tournassat, C., Gailhanou, H., Crouzet, C., Braibant, G., Gautier, A., Gaucher, E.C., 2009. Cation exchange selectivity coefficient values on smectite and mixed-layer illite/smectite minerals. Soil Science Society of America Journal 73, 928–942. https://doi.org/10.2136/sssaj2008.0285.
Underwood, G., 2010. Exopolymers (extracellular polymeric substances) in diatom dominated marine sediment biofilms. In: Seckbach, J., Oren, A. (Eds.), Cellular Origin, Life in Extreme Habitats and Astrobiology. Springer, Netherlands, pp. 287–300.
Urbani, R., Sist, P., Pletikapic, G., Radic, T.M., Svetlicc, V., Zutic, V., 2012. Diatom polysaccharides: extracellular production, isolation and molecular characterization. In: Karunaratne, D.N. (Ed.), The Complex World of Polysaccharides. INTECH, Croatia, pp. 345–367 https://doi.org/10.5772/51251.
Weischet, W., 1996. Regionale Klimatologic. Die neue Welt. Tcubner, Stuttcart, p. 468.
Welton, J.E., 2003. SEM Petrology Atlas: Methods in Exploration Series No. 4. vol. 2. American Association on Petroleum Geologists, p. 240.
White, A.F., Blum, A.E., 1995. Effects of climate on chemical weathering in watersheds. Geochimica et Cosmochimica Acta 59, 1729–1747. https://doi.org/10.1016/0016-7037(95)00078-E.
Williams, W., 2002. Environmental threats to salt lakes and the likely status of inland saline ecosystems in 2025. Environmental Conservation 29, 154–167. https://doi.org/10.1017/S0376892902000103.
Wilson, M., 2004. Weathering of the primary rock-forming minerals: processes, products and rates. Clay Minerals 39, 233–266. https://doi.org/10.1180/0009855043930133.
Winslow, M.A., 1983. Clastic dike swarms and the structural evolution of the foreland fold and thrust belt of the southern Andes. Geological Society of America Bulletin 1073–1080.
Wright, V.P., Barnett, A.J., 2015. An abiotic model for the development of textures in some South Atlantic early Cretaceous lacustrine carbonates. Geological Society, London, Special Publications 418, 209–219.
Zhang, F., Xu, H., Konishi, H., Roden, E.E., 2010. A relationship between d104 value and composition in the calcite-disordered dolomite solid-solution series. American Mineralogist 95, 1650–1656. https://doi.org/10.2138/am.2010.3414.
Zolitschka, B., Schäbitz, F., Lücke, A., Corbella, H., Ercolano, B., Fey, M., Haberzettl, T., Janssen, S., Maidana, N., Mayr, C., Ohlendorf, C., 2006. Crater lakes of the Pali Aike Volcanic Field as key sites of paleoclimatic and paleoecological reconstructions in southern Patagonia, Argentina. Journal of South American Earth Sciences 21, 294–309. https://doi.org/10.1016/j.jsames.2006.04.001.